

# High-temperature superconductivity of ternary $\text{Ca}_4\text{B}_x\text{C}_{23-x}$ clathrates at moderate pressure

Peng Chen <sup>1</sup>, Zepeng Wu <sup>1</sup>, Yang Sun <sup>1</sup>, Tie-Yu Lü,<sup>1</sup> Xinrui Cao <sup>1,2</sup>, Zi-zhong Zhu <sup>1,2</sup> and Shunqing Wu <sup>1,\*</sup>

<sup>1</sup>Department of Physics, OSED, Key Laboratory of Low Dimensional Condensed Matter Physics

(Department of Education of Fujian Province), [Xiamen University](#), Xiamen 361005, China

<sup>2</sup>Fujian Provincial Key Laboratory of Theoretical and Computational Chemistry, [Xiamen University](#), Xiamen 361005, China



(Received 17 August 2024; revised 28 October 2024; accepted 25 November 2024; published 17 December 2024)

The synthesis of  $\text{SrB}_3\text{C}_3$  and the research on its analogs demonstrate the high-temperature superconductivity of ternary metal-boron-carbon clathrates at ambient or moderate pressure. Here, we explore the stability and superconductivity of calcium-doped and boron-substituted type-VIII carbon clathrates  $\text{Ca}_4\text{B}_x\text{C}_{23-x}$  ( $x = 0 - 23$ ) at 25–100 GPa. Based on the structural features and density functional theory (DFT) calculations, we screened 8 388 608 possible B-decorated structures and ultimately identified five thermodynamically metastable superconductors. Among them,  $\text{Ca}_4\text{B}_{10}\text{C}_{13}$  (space group  $I\bar{4}3m$ ) exhibited the highest  $T_c$  of  $\sim 101 - 109$  K, between 25 and 100 GPa. The high  $T_c$  of  $\text{Ca}_4\text{B}_{10}\text{C}_{13}$  originates from strong electron-phonon coupling caused by phonon softening and high density of states at the Fermi level. Our findings suggest that metal-doped and boron-substituted carbon clathrates are promising high-temperature superconductors at moderate pressure.

DOI: [10.1103/PhysRevB.110.214106](https://doi.org/10.1103/PhysRevB.110.214106)

## I. INTRODUCTION

In recent years, a series of high-temperature hydrogen-rich superconductors have been theoretically predicted and successfully synthesized, such as  $\text{CaH}_6$  (215 K, 172 GPa [1,2]),  $\text{YH}_9$  (243 K, 201 GPa [3,4]),  $\text{LaH}_{10}$  ( $\sim 250$  K, 170 GPa [5,6]). The common structural feature of these hydrogen-rich high-temperature superconductors is a cage-like structure formed by hydrogen atoms. However, the extremely high stabilizing pressure required for hydrogen-rich superconductors limits their practical application. Consequently, researchers have been working to explore high-temperature superconductors at lower pressure. For example, a series of compounds, represented by  $\text{Mg}_2\text{IrH}_6$ , have been predicted to be high- $T_c$  superconductors at ambient pressure very recently [7–9]. Additionally, a series of few-hydrogen compounds have also been expected to be high-temperature superconductors at ambient pressure, such as  $\text{Al}_4\text{H}$  ( $\sim 54$  K [10]),  $(\text{Be}_4)_2\text{H}$  ( $\sim 72 - 84$  K [11]), and  $\text{MgHCu}_3$  ( $\sim 42$  K [12]).

Another effective approach is to replace H with other light elements, such as B, C, and N. Some binary carbides were predicted to have a high  $T_c$  at ambient pressure. For instance,  $\text{NaC}_6$  in the sodalite structure has been predicted as a potential superconductor with  $T_c \sim 116$  K [13].  $\text{MC}_6$  (where  $M$  represents other metals replacing Na) with the same structure has also been theoretically studied [14,15]. It was found that the compounds with a carbon-cage-network structure have higher  $T_c$  values than those carbon-based materials without a cage. Nonetheless, the high formation energy characteristic poses a significant challenge to synthesis. Zeng *et al.* theoretically studied Li-filled, B-substituted carbon clathrates and found that the strategy of boron substitution could improve

the thermodynamic stability of carbon clathrate frameworks [16]. Recently,  $\text{SrB}_3\text{C}_3$  ( $Pm - 3n$ ) was successfully synthesized at 50 GPa and was recovered to ambient pressure under inert conditions with  $T_c$  of  $\sim 20$  K (27–43 K) at 40 GPa by experiment (theory) [17,18].  $\text{SrB}_3\text{C}_3$  consists of a  $sp^3$ -bonded framework with equal amounts of boron and carbon in the sodalite structure. The substitution of half of the C atoms with B provides  $p$ -type doping which maintains its dynamic stability at 0–200 GPa and thermodynamic stability at 50–200 GPa [17].

Due to the host-guest structure of boron-carbon clathrates, it is a promising path to enhance the  $T_c$  by tuning guest atoms or host framework of clathrates. For example,  $\text{CaB}_3\text{C}_3$  and  $\text{BaB}_3\text{C}_3$  with similar structures to  $\text{SrB}_3\text{C}_3$  were predicted to be dynamically stable at ambient pressure with  $T_c$  of 48 K [19] and 43 K [20], respectively. Additionally, Rb-doped  $\text{SrB}_3\text{C}_3$  was predicted to have a high  $T_c$  above 70 K [21,22]. Other boron-carbon clathrates as the analogs of  $\text{SrB}_3\text{C}_3$  have also been predicted to exist high values of  $T_c$  at ambient pressure, such as  $\text{KPbB}_6\text{C}_6$  ( $T_c \sim 88$  K [23]),  $\text{RbYbB}_6\text{C}_6$  ( $T_c \sim 67$  K [24]), and  $\text{RbBaB}_6\text{C}_6$  ( $T_c \sim 68$  K [24]). Very recently,  $\text{SrNH}_4\text{B}_6\text{C}_6$  was designed by doping  $\text{SrB}_3\text{C}_3$  with small hydride units  $\text{NH}_4$ . This modification effectively improved  $T_c$  to 73 K at 1 atm. Its analog  $\text{PbNH}_4\text{B}_6\text{C}_6$  was predicted with a  $T_c$  of  $\sim 86$  K at 1 atm [25]. On the other hand,  $\text{LaH}_{10}$ -like host frameworks have been used to construct boron-carbon clathrates of the type  $Fm\bar{3}m\text{-XB}_2\text{C}_8$  (where  $X$  is metal elements) [26,27], which possess  $T_c$  around or above liquid nitrogen temperature at ambient pressure. Additionally, some boron-nitrogen and boron-silicon clathrates have been predicted to be superconductors at ambient pressure, such as  $\text{Al}(\text{BN})_6$  ( $T_c \sim 47$  K [28]),  $\text{Al}_2(\text{BN})_6$  ( $T_c \sim 72$  K [29]),  $\text{RbB}_3\text{Si}_3$  ( $T_c \sim 14$  K [30]).

These studies suggest that B-C clathrates have great potential for exploration in the search for high-temperature

\*Contact author: [wsq@xmu.edu.cn](mailto:wsq@xmu.edu.cn)

superconductors at ambient or moderate pressure. Many metastable carbon clathrate frameworks have been theoretically investigated [31–39], such as the  $sp^3$ -bonded type-VIII carbon clathrate derived from  $\text{Ba}_8\text{Ga}_{16}\text{Sn}_{30}$  [40]. This raises the question of whether B-C clathrate superconductors could be designed using a similar strategy based on other  $sp^3$ -bonded carbon clathrates. We also noted that a recent study predicted a thermodynamically stable  $\text{Ca}_8\text{B}_{16}\text{C}_{30}$  at 50 GPa [41]. However, it is a semiconductor with a band gap of  $\sim 2.5$  eV. In other studies of Ca-B-C systems, while some phases are predicted to be superconductors, their  $T_c$  are below 40 K at ambient pressure, such as  $\text{CaB}_2\text{C}_4$  ( $T_c \sim 1.7$  K),  $\text{CaB}_4\text{C}_2$  ( $T_c \sim 15$  K) [42],  $\text{Ca}_2\text{BC}_{11}$  ( $T_c \sim 8.9$  K),  $\text{CaBC}_5$  ( $T_c \sim 5.2$  K), and  $\text{CaB}_3\text{C}_3$  ( $T_c \sim 26.1$  K) [43]. Thus, we look forward to further exploring clathrates with high  $T_c$  in the Ca-B-C ternary system with a type-VIII carbon clathrate framework.

In this paper, based on condition screening and density functional theory (DFT) calculations, we explored the stability and superconductivity of ternary  $\text{Ca}_4\text{B}_x\text{C}_{23-x}$  ( $x = 0\text{--}23$ ) clathrates at 25–100 GPa. The structure motif used is the type-VIII carbon clathrates from Refs. [31,40]. Boron atoms were introduced by partially replacing carbon sites, and all possible replacement sites were considered for  $\text{Ca}_4\text{B}_x\text{C}_{23-x}$  with varying boron contents. After screening the structural features and performing DFT calculations, we identified five thermodynamically metastable, dynamically stable, and metallic phases at 25–100 GPa. Their superconductivity was assessed using DFPT (density functional perturbation theory) calculations, such as  $\text{Ca}_4\text{B}_{10}\text{C}_{13}$  with  $T_c$  above 100 K at 25–100 GPa.

## II. COMPUTATIONAL DETAILS

Structure relaxations and electronic properties were carried out using the Perdew-Burke-Ernzerhof (PBE) generalized gradient approximation (GGA) [44] in the framework of the projector augmented wave (PAW) [45] method as implemented in the VASP code [46]. The valence electrons of  $3s^2 3p^6 4s^2$ ,  $2s^2 2p^1$ , and  $2s^2 2p^2$  for Ca, B, and C were used in the PAW method, respectively. The plane-wave basis set with an energy cutoff of 600 eV and a Monkhorst-Pack Brillouin zone (BZ) sampling density of  $2\pi \times 0.015 \text{ \AA}^{-1}$  were employed in the structure relaxations and self-consistent calculations. The structural optimization was performed using the conjugate gradient algorithm with variable cell shapes, and the convergence threshold is  $-0.01 \text{ eV/\AA}$  for the atomic force. Phonon calculations were carried out in the finite displacement method using the VASP package coupled to the PHONOPY code [47]. For these calculations,  $2 \times 2 \times 2$  supercells with  $\sim 216$  atoms and a Monkhorst-Pack BZ sampling density of  $2\pi \times 0.025 \text{ \AA}^{-1}$  were employed.

Within the framework of DFPT [48], electron-phonon coupling (EPC) was calculated by ultrasoft pseudopotentials (USPP) [49] with PBE functional implemented in the QUANTUM ESPRESSO package (QE) [50,51]. The same configurations of valence electrons as used in PAW were applied in USPP. The kinetic energy cutoffs were 70 Ry for wave functions and 560 Ry for charge density. The calculating electronic structures of  $\text{Ca}_4\text{B}_{10}\text{C}_{13}$  under different pressures performed pretty consistent results between VASP and QE in

Supplemental Material Note S1 [52]. Q-point meshes with  $3 \times 3 \times 3$  were used for DFPT calculation. Self-consistent electron density and EPC were calculated by employing a  $6 \times 6 \times 6$   $k$ -point mesh, and a dense  $12 \times 12 \times 12$  grid was used for evaluating an accurate electron-phonon interaction matrix. We also tested  $q$ -point meshes with  $4 \times 4 \times 4$ , and the results of EPC were similar to those obtained with the  $3 \times 3 \times 3$  meshes.

The calculations of  $T_c$  are based on the Eliashberg spectrum function defined as [53–55]

$$\alpha^2 F(\omega) = \frac{1}{2\pi N(E_F)} \sum_{qv} \frac{\gamma_{qv}}{\hbar\omega_{qv}} \delta(\omega - \omega_{qv}), \quad (1)$$

where  $N(E_F)$  is the density of states (DOS) at the Fermi level,  $\omega_{qv}$  represents the phonon frequency of the mode  $v$  with wave vector  $q$ , and  $\gamma_{qv}$  is the phonon linewidth defined as

$$\gamma_{qv} = \frac{2\pi\omega_{qv}}{\Omega_{\text{BZ}}} \sum_{i,j} \int d^3k |g_{k,qv}^{i,j}|^2 \delta(\varepsilon_{i,q} - E_F) \delta(\varepsilon_{j,k+q} - E_F). \quad (2)$$

Here,  $g_{k,qv}^{i,j}$  is the EPC matrix element, and  $\Omega_{\text{BZ}}$  is the volume of the Brillouin zone. The EPC constant can be determined as

$$\lambda = \sum_{qv} \frac{\gamma_{qv}}{\pi \hbar N(E_F) \omega_{qv}^2} = 2 \int \frac{\alpha^2 F(\omega)}{\omega} d\omega. \quad (3)$$

For EPC constant  $\lambda < 1.5$ ,  $T_c$  was firstly estimated from the McMillan-Allen-Dynes (MAD) formula [53,54]:

$$T_c = \frac{\omega_{\log}}{1.2} \exp\left[-\frac{1.04(1+\lambda)}{\lambda - \mu^*(1+0.62\lambda)}\right]. \quad (4)$$

For the strong EPC system with  $\lambda > 1.5$ ,  $T_c$  was corrected by the Allen-Dynes–corrected McMillan formula [55]:

$$T_c = f_1 f_2 \frac{\omega_{\log}}{1.2} \exp\left[-\frac{1.04(1+\lambda)}{\lambda - \mu^*(1+0.62\lambda)}\right], \quad (5)$$

where the correction factors  $f_1$ ,  $f_2$  were defined by  $\lambda$ ,  $\mu^*$ ,  $\omega_{\log}$ , and mean-square frequency  $\omega_2$ . Here, the renormalized Coulomb potential  $\mu^* = 0.10$ , which is a conventional setting for B-C clathrates [19,23], was used. The logarithmic average frequency  $\omega_{\log}$  is computed as

$$\omega_{\log} = \exp\left(\frac{2}{\lambda} \int \frac{\alpha^2 F(\omega)}{\omega} \ln \omega d\omega\right). \quad (6)$$

We also estimated the superconducting gap and  $T_c$  using the Migdal-Eliashberg (ME) approach by numerically solving isotropic Eliashberg equations [56,57]. For the details of the computational method, refer to Refs. [58–60].

## III. RESULTS AND DISCUSSION

### A. Structure screening

The space group of type-VIII clathrate is  $I\bar{4}3m$ , and the carbon atoms occupy the  $2a$  (0, 0, 0),  $8c$  ( $x_c, x_c, x_c$ ),  $12d$  ( $1/4, 1/2, 0$ ), and  $24g$  ( $x_g, x_g, z_g$ ) Wyckoff positions, where  $x_c \approx 0.137$ ,  $x_g \approx 0.586$ , and  $z_g \approx 0.856$ . As shown in Fig. 1(a), there are eight [ $3^4 4^3 5^9$ ] cages (pentadecahedron) and three small [ $3^4 4^4$ ] (octahedron) voids in the conventional cell of type-VIII clathrate with 46 carbon atoms. In

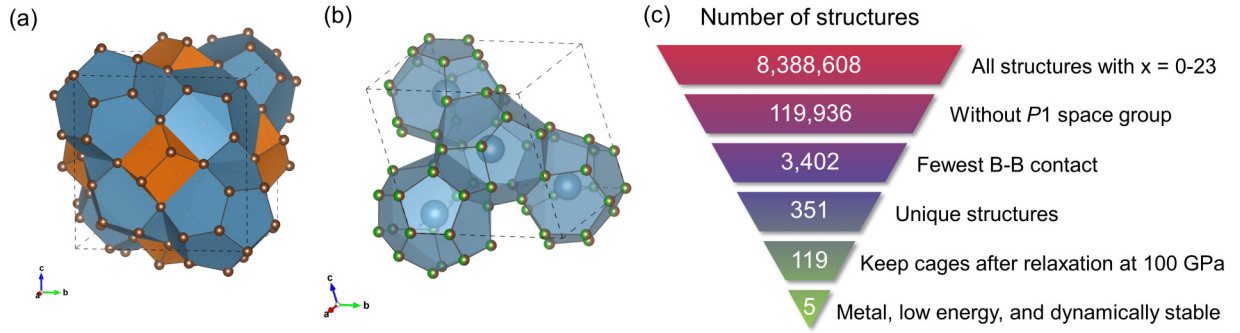


FIG. 1. (a) Crystal structure of type-VIII clathrate from Refs. [31,40], where the C atoms are shown as brown spheres. The blue polyhedrons represent  $[3^3 4^3 5^9]$  cages, and the orange ones represent small  $[3^4 4^4]$  voids. The cage representation was the same as Ref. [31], e.g.,  $[3^3 4^3 5^9]$  means a cage with 3 three-membered rings, 3 four-membered rings, and 9 five-membered rings. (b) Crystal structure of  $\text{Ca}_4\text{B}_x\text{C}_{23-x}$  ( $x = 0 - 23$ ), where the Ca and B/C atoms are shown as blue and green/brown spheres, respectively. (c) Number of structures in  $\text{Ca}_4\text{B}_x\text{C}_{23-x}$  with possible B substitution sites and the number of structures remaining after screening under different conditions.

the following study, the primitive cell with 23 atoms of type-VIII clathrate was used to construct B-C clathrates with four  $[3^3 4^3 5^9]$  cages. The shortest distance between the center point and the vertices of the  $[3^4 4^4]$  carbon cage is only 1.25 Å at 0 GPa, which is shorter than the other carbon cages (1.63 Å–2.55 Å) [31]. Considering the smaller capacity of  $[3^4 4^4]$  voids, we constructed B-C clathrates of  $\text{Ca}_4\text{B}_x\text{C}_{23-x}$  by doping calcium atoms only in  $[3^3 4^3 5^9]$  cages and boron substitution as shown in Fig. 1(b).

At a definite  $x$  value, the number of total possible structures of  $\text{Ca}_4\text{B}_x\text{C}_{23-x}$ ,  $N_x$ , is given by

$$N_x = C_{23}^x = \frac{23!}{(23-x)!x!}. \quad (7)$$

As shown in Fig. 1(c), the sum of  $N_x$  from  $x = 0$  to  $x = 23$  is 8 388 608, which is too immense to direct DFT calculations. In previous studies on boron-substituted carbon clathrates, it was found that B-B contact was energetically disadvantageous [16,41], and those with  $P1$  space-group symmetry were rarely observed as ground states [16,41,61,62]. Thus, to decrease  $N_x$ , we set up filters to remove structures with  $P1$  space group symmetry and only reserve those structures with the fewest B-B contact. To test the rationality of such filters, we computed the enthalpies of  $\text{Ca}_4\text{B}_{10}\text{C}_{13}$  with  $P1$  space-group symmetry at 100 GPa (see Supplemental Note S2 [52]). We found that the B-B contacts are energetically unfavorable. Here, the structures of  $\text{Ca}_4\text{B}_x\text{C}_{23-x}$  without B-B contact can be found when  $x \leq 10$ , but they will inevitably have B-B contact when  $x \geq 11$ . As shown in Fig. 1(c), the filters effectively reduce the number of possible structures to 3402, and it can be further diminished to 351 after removing the symmetry equivalence structures. The detailed number of remaining structures can be found in Table S1 [52].

The full relaxation of these structures was performed at 25, 50, and 100 GPa for these 351 structures. We found that some of these structures failed to maintain the cage-like structure or had local defects, which reflected the structural instability caused by the corresponding boron substitution scheme. However, we were only interested in those cage-like structures, so we set up a criterion with C-C bond length  $< 2.1$  Å, B-C bond length  $< 2.2$  Å, and B-B bond length  $< 2.3$  Å to identify the cage-like structures. Under the screening of this criterion, 70,

85, and 119 cage structures were left at 25, 50, and 100 GPa, respectively.

### B. Phase stability

To evaluate the thermodynamic stability of the selected structures after structure screening, we first calculated the formation enthalpy  $\Delta H$  at 25–100 GPa, which is defined as

$$\Delta H = \frac{H(\text{Ca}_4\text{B}_x\text{C}_{23-x}) - 4H(\text{Ca}) - xH(\text{B}) - (23-x)H(\text{C})}{27}, \quad (8)$$

where  $H(\text{Ca}_4\text{B}_x\text{C}_{23-x})$  is the total enthalpy of the  $\text{Ca}_4\text{B}_x\text{C}_{23-x}$  compounds. Here,  $H(\text{Ca})$ ,  $H(\text{B})$ , and  $H(\text{C})$  are the enthalpies of the ground states of Ca, B, and C, respectively, at corresponding pressure (see Table S2 [52]). As shown in Fig. 2(a), when  $x \leq 7$  and  $x \geq 11$ , there are a lot of relaxed structures that could not keep cage characters, which are labeled with a cross. Besides, focusing on those cage structures, we found that  $\Delta H$  shows a decreasing trend with  $x$  from 0 to 8 and turns to be increasing when  $x$  is from 8 to 23 at different pressures. Besides,  $\text{Ca}_4\text{B}_x\text{C}_{23-x}$  has lower values of  $\Delta H$  with pressure increasing, and the lowest  $\Delta H$  reaches -0.524 eV/atom at 100 GPa in  $x = 8$ .

Next, we further verified the thermodynamic stability for the cage structures by calculating the convex hull of the Ca-B-C system at 25, 50, and 100 GPa, as shown in Fig. S5 [52], and the results of calculated enthalpy above the convex hull ( $E_d$ ) were summarized in Fig. 2(b). A similar V-shaped trend of first decreasing and then increasing with growing  $x$  can also be observed in the  $E_d$  of  $\text{Ca}_4\text{B}_x\text{C}_{23-x}$ , and the low point of  $E_d$  is around  $x = 8$  at different pressures. This indicates that those structures with a boron content close to  $\text{Ca}_4\text{B}_8\text{C}_{15}$  (insulators, see Fig. S6 [52]) are energy favorable. And the pressure decreases  $E_d$  of  $\text{Ca}_4\text{B}_x\text{C}_{23-x}$ , which is consistent with other studies about B-C clathrates [16,17,41,63]. Here, we are more interested in those structures that have lower  $E_d$  under pressure, which are more likely to be synthesized at high pressure [17,63]. As discussed in Refs. [64,65], many metastable inorganic materials can be synthesized within a specific energy range. There are also some metastable M-B, M-C, and M-B-C (M means metal element) compounds



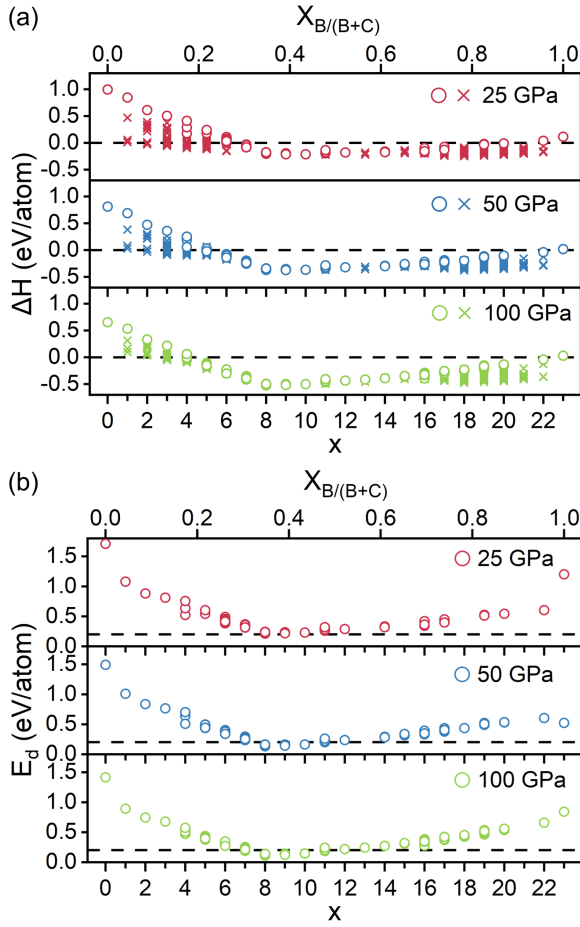


FIG. 2. (a) Calculated formation enthalpy of the uniquely relaxed phases without P1 space-group symmetry and with the fewest B-B contacts at 25, 50, and 100 GPa. The relaxed structures with (without) keeping intact cage characters are labeled with a circle (cross). (b) Calculated enthalpy above convex hull ( $E_d$ ) of the uniquely relaxed phases with cagelike structures (cage structure) at 25, 50, and 100 GPa. In (a) and (b), the lower  $x$  axis is the value of  $x$  in  $\text{Ca}_4\text{B}_x\text{C}_{23-x}$ , and the upper  $x$  axis is the ratio of B to (B + C) in  $\text{Ca}_4\text{B}_x\text{C}_{23-x}$  (labeled as  $X_{B/(B+C)}$ ). The dashed line in (b) indicates the 0.2 eV/atom threshold to identify the phases with low enthalpy. Note that we excluded the data points of structures that did not maintain the cage structure after relaxation.

that have been experimentally synthesized, but we confirmed that they are theoretically thermodynamic metastable. For example,  $I4_1/acd$   $\text{Na}_2\text{C}_2$  [66],  $Fm\bar{3}m$   $\text{ZrB}$  [67], and  $P\bar{4}m2$   $\text{Li}_2\text{B}_2\text{C}$  [68] have been experimentally synthesized under certain conditions. And our calculations indicate that  $I4_1/acd$   $\text{Na}_2\text{C}_2$  ( $E_d = 0.224$  eV/atom),  $Fm\bar{3}m$   $\text{ZrB}$  ( $E_d = 0.378$  eV/atom), and  $P\bar{4}m2$   $\text{Li}_2\text{B}_2\text{C}$  ( $E_d = 0.243$  eV/atom) are metastable compounds. Given these examples, we may not be able to rule out the synthesizability of those structures with  $E_d > 0.2$  eV/atom. However, to screen out the more synthesizable structures efficiently, we used a criterion of  $E_d < 0.2$  eV/atom at 100 GPa to screen superconducting candidates. As shown in Fig. 2(b), 2, 2, 1, and 2 structures meet the criterion of  $E_d$  when  $x = 7, 9, 10$ , and 11, respectively. The phases with  $x = 8$  were not considered because they were insulators as shown in Fig. S6 [52]. So, we get

seven metallic structures with  $E_d < 0.2$  eV/atom at 100 GPa, which were  $\text{Ca}_4\text{B}_7\text{C}_{16}$  ( $I\bar{4}3m$ ),  $\text{Ca}_4\text{B}_7\text{C}_{16}$  ( $R3m$ ),  $\text{Ca}_4\text{B}_9\text{C}_{14}$  ( $R3m$ ),  $\text{Ca}_4\text{B}_9\text{C}_{14}$  ( $I\bar{4}$ ),  $\text{Ca}_4\text{B}_{10}\text{C}_{13}$  ( $I\bar{4}3m$ ),  $\text{Ca}_4\text{B}_{11}\text{C}_{12}$  ( $Cm$ ), and  $\text{Ca}_4\text{B}_{11}\text{C}_{12}$  ( $C2$ ), and their detailed structure information was shown as in Table S5 [52].

Then we evaluated the dynamic stability of seven structures, and their phonon spectra at 25, 50, and 100 GPa are shown in Figs. S7–S9 [52]. The results showed that five phases of  $R3m$   $\text{Ca}_4\text{B}_9\text{C}_{14}$ ,  $I\bar{4}$   $\text{Ca}_4\text{B}_9\text{C}_{14}$ ,  $I\bar{4}3m$   $\text{Ca}_4\text{B}_{10}\text{C}_{13}$ ,  $Cm$   $\text{Ca}_4\text{B}_{11}\text{C}_{12}$ , and  $C2$   $\text{Ca}_4\text{B}_{11}\text{C}_{12}$  were harmonic dynamically stable from 25 to 100 GPa, but the other two phases of  $\text{Ca}_4\text{B}_7\text{C}_{16}$  were dynamically unstable at the harmonic level from 25 to 100 GPa for the imaginary phonon frequency. Considering the anharmonic effect in the light element system [69–71], these two  $\text{Ca}_4\text{B}_7\text{C}_{16}$  phases might be dynamically stable when the anharmonic effect is taken into account. However, it was beyond the scope of this study. So, in the following study, we excluded two  $\text{Ca}_4\text{B}_7\text{C}_{16}$  phases and only considered the other five phases as shown in Fig. 3.

### C. Electron-phonon coupling and superconductivity

For these five metastable phases, we first performed the fast frozen-phonon calculation of the zone-center EPC strength to evaluate the superconductivity [72]. This method has been successfully applied in ternary metal diborides and hydrogen-rich compositions [60,73]. As shown in Table I, three phases of  $R3m$   $\text{Ca}_4\text{B}_9\text{C}_{14}$ ,  $I\bar{4}$   $\text{Ca}_4\text{B}_9\text{C}_{14}$ , and  $I\bar{4}3m$   $\text{Ca}_4\text{B}_{10}\text{C}_{13}$  had high  $\lambda_\Gamma$  from 0.40 to 0.49 at 50 GPa, which indicated their potential strong EPC strength compared to the  $\lambda_\Gamma = 0.44$  of  $\text{MgB}_2$  [72]. We then performed the DFPT calculations to further demonstrate their superconductivity and evaluated the  $T_c$  by MAD formula and Migdal-Eliashberg approach as shown in Table I. Their superconducting energy gap is shown in Fig. S10 [52]. As is expected, the full Brillouin zone EPC  $\lambda$  of 0.62 for  $R3m$   $\text{Ca}_4\text{B}_9\text{C}_{14}$  and 0.70 for  $I\bar{4}$   $\text{Ca}_4\text{B}_9\text{C}_{14}$  are comparable to  $\text{MgB}_2$  ( $\lambda \sim 0.7$ ) [74] at 0 GPa and  $\text{SrB}_3\text{C}_3$  ( $\lambda \sim 0.7$ ) [18] at 50 GPa. However,  $Cm$   $\text{Ca}_4\text{B}_{11}\text{C}_{12}$  and  $C2$   $\text{Ca}_4\text{B}_{11}\text{C}_{12}$  had relatively small values of  $\lambda_\Gamma$ , but they still performed considerable  $\lambda$  of 0.68 and 1.00 at 50 GPa, respectively, which indicates those phonon modes away from the zone center play an important role in EPC for these two phases. Remarkably,  $\text{Ca}_4\text{B}_{10}\text{C}_{13}$  possesses strong EPC and high superconduct temperature at 50 GPa and has the highest  $\lambda$  of 1.30 and  $T_c$  of 101 K above liquid nitrogen temperature. Compared with such a high  $T_c$  of  $\text{Ca}_4\text{B}_{10}\text{C}_{13}$ , the  $T_c$  difference between the two  $\text{Ca}_4\text{B}_9\text{C}_{14}$  phases and between the two  $\text{Ca}_4\text{B}_{11}\text{C}_{12}$  phases were all smaller, indicating that the boron contents played a more important role in  $T_c$  than the distribution of boron.

To further understand the origin of such high  $\lambda$  and  $T_c$  values of  $\text{Ca}_4\text{B}_{10}\text{C}_{13}$ , we plotted its phonon spectrum, projected phonon density of states (PHDOS), Eliashberg spectral function  $\alpha^2F(\omega)$ , EPC integral  $\lambda(\omega)$ , fat electron band structure, projected density of states (PDOS), and total density of states (TDOS) at 50 GPa in Fig. 4. For comparison, the results of ground states of  $R3m$   $\text{Ca}_4\text{B}_9\text{C}_{14}$ , and  $Cm$   $\text{Ca}_4\text{B}_{11}\text{C}_{12}$  at 50 GPa were also plotted in Fig. 4, and the results of  $I\bar{4}$   $\text{Ca}_4\text{B}_9\text{C}_{14}$  and  $C2$   $\text{Ca}_4\text{B}_{11}\text{C}_{12}$  can be found in Figs. S11–S13 [52]. Firstly, we observed the phonon modes dominated by the B-C covalent framework strongly coupled with the high-density B-C

TABLE I. Space group, DOS at the Fermi level  $[N(E_F)]$ , zone-center EPC  $\lambda_\Gamma$ , full Brillouin zone EPC  $\lambda$ , logarithmic average frequency  $\omega_{\log}$ , and  $T_c$  of  $R3m$   $\text{Ca}_4\text{B}_9\text{C}_{14}$ ,  $I\bar{4}$   $\text{Ca}_4\text{B}_9\text{C}_{14}$ ,  $I\bar{4}3m$   $\text{Ca}_4\text{B}_{10}\text{C}_{13}$ ,  $Cm$   $\text{Ca}_4\text{B}_{11}\text{C}_{12}$ , and  $C2$   $\text{Ca}_4\text{B}_{11}\text{C}_{12}$  at 50 GPa.  $T_c$  is estimated using the MAD formula  $T_{c\_MAD}$  and Migdal-Eliashberg approach  $T_{c\_ME}$  by setting the screened Coulomb potential  $\mu^* = 0.10$ .

| Structure                               | Space group  | $N(E_F)$ states/(eV f.u.) | $\lambda_\Gamma$ | $\lambda$ | $\omega_{\log}$ (K) | $T_{c\_MAD}$ (K) | $T_{c\_ME}$ (K) |
|---|--------------|---------------------------|------------------|-----------|---------------------|------------------|-----------------|
| $\text{Ca}_4\text{B}_9\text{C}_{14}$    | $R3m$        | 8.53                      | 0.46             | 0.62      | 964                 | 24               | 30              |
| $\text{Ca}_4\text{B}_9\text{C}_{14}$    | $I\bar{4}$   | 8.75                      | 0.40             | 0.70      | 985                 | 34               | 41              |
| $\text{Ca}_4\text{B}_{10}\text{C}_{13}$ | $I\bar{4}3m$ | 9.12                      | 0.49             | 1.30      | 870                 | 85               | 101             |
| $\text{Ca}_4\text{B}_{11}\text{C}_{12}$ | $Cm$         | 3.01                      | 0.12             | 0.76      | 642                 | 27               | 32              |
| $\text{Ca}_4\text{B}_{11}\text{C}_{12}$ | $C2$         | 5.28                      | 0.24             | 1.00      | 429                 | 30               | 35              |

covalent electrons at the Fermi level in all three phases as shown in Fig. 4, which brings the main contribution to their EPC and is the same with other B-C clathrate superconductors [18–23]. Among them, the phonon modes that played a major role in EPC are mainly concentrated in middle- and high-frequency regions, such as the breathing modes at  $\Gamma$  point as shown in Fig. S14 [52]. Especially, we noted that  $\text{Ca}_4\text{B}_{10}\text{C}_{13}$  has significantly softened phonon modes accompanied by large phonon linewidth in the medium frequency region compared with  $R3m$   $\text{Ca}_4\text{B}_9\text{C}_{14}$ , as shown in Figs. 4(a) and 4(b). Note that the softened phonons here mean the overall frequency descent behavior of many phonon modes in middle-frequency regions, as discussed in Supplemental Material Note S3 [52]. Because of the large phonon linewidth of the phonon modes dominated by B and C in the middle-frequency regions, the Eliashberg spectral functions  $\alpha^2F(\omega)$  of  $R3m$   $\text{Ca}_4\text{B}_9\text{C}_{14}$  and  $\text{Ca}_4\text{B}_{10}\text{C}_{13}$  all show a peaklike distribution in middle-frequency regions. If we integrate Eq. (3) in the range of 0–600  $\text{cm}^{-1}$ , we find that the contribution to  $\lambda$  of  $R3m$   $\text{Ca}_4\text{B}_9\text{C}_{14}$  is 0.124 in this range (see Table S3 [52]). In contrast,  $\text{Ca}_4\text{B}_{10}\text{C}_{13}$  has a high proportion of integral  $\lambda$  of 0.559 in the range of 0–600  $\text{cm}^{-1}$  due to the softened phonon modes. Such phonon softening leads to a higher total EPC constant

$\lambda = 1.30$  and  $T_c = 101$  K of  $\text{Ca}_4\text{B}_{10}\text{C}_{13}$  than  $R3m$   $\text{Ca}_4\text{B}_9\text{C}_{14}$  at 50 GPa. This analysis illustrates that  $\text{Ca}_4\text{B}_{10}\text{C}_{13}$  with higher B content leads to significant phonon softening compared to  $R3m$   $\text{Ca}_4\text{B}_9\text{C}_{14}$ , which enhances EPC and improves  $T_c$ .

In addition, the high  $N(E_F)$  is also an important factor leading to the high  $T_c$  of  $\text{Ca}_4\text{B}_{10}\text{C}_{13}$ . As shown in Figs. 4(d)–4(f), the increase of boron content has the effect of hole doping, which significantly regulates the electronic band structure of these three phases. The Van Hove singularity (VHS) lies on the Fermi level at the F point for  $R3m$   $\text{Ca}_4\text{B}_9\text{C}_{14}$ , and the multiple bands cross the Fermi level for  $\text{Ca}_4\text{B}_{10}\text{C}_{13}$ , leading to their high  $N(E_F)$ . As shown in Eq. (3),  $\lambda$  appears to have a negative correlation with  $N(E_F)$ . However, there is a positive correlation between  $\gamma_{qv}$  and the square of  $N(E_F)$ ; as shown in Eq. (2), the sum contains the product of two  $\delta$  functions. So, it actually results in a positive correlation between  $\lambda$  and  $N(E_F)$ , and  $\lambda$  can be written in the form of  $\lambda = \frac{N(E_F)\langle I^2 \rangle}{M\langle \omega^2 \rangle}$ , as described in Refs. [53,55]. Therefore, the high  $N(E_F)$  favor large  $\lambda$  and  $T_c$ . As shown in Figs. 4(c) and 4(f), although  $Cm$   $\text{Ca}_4\text{B}_{11}\text{C}_{12}$  has more softened phonons, their contributions to EPC were greatly hindered due to the low  $N(E_F)$ . This is also the key to why the  $T_c$  of  $Cm$   $\text{Ca}_4\text{B}_{11}\text{C}_{12}$  is much lower than that of  $\text{Ca}_4\text{B}_{10}\text{C}_{13}$  at 50 GPa. Given the above, it can be concluded

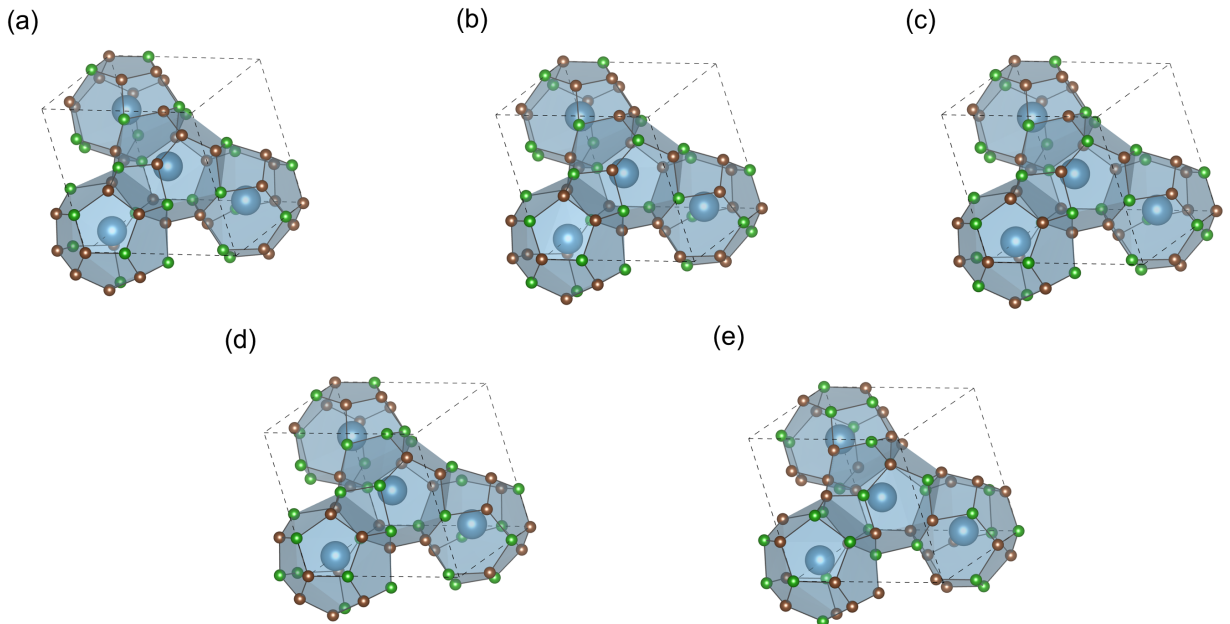


FIG. 3. Crystal structures of (a)  $R3m$   $\text{Ca}_4\text{B}_9\text{C}_{14}$ , (b)  $I\bar{4}$   $\text{Ca}_4\text{B}_9\text{C}_{14}$ , (c)  $I\bar{4}3m$   $\text{Ca}_4\text{B}_{10}\text{C}_{13}$ , (d)  $Cm$   $\text{Ca}_4\text{B}_{11}\text{C}_{12}$ , and (e)  $C2$   $\text{Ca}_4\text{B}_{11}\text{C}_{12}$  at 50 GPa, where the Ca, B, and C atoms are shown as blue, green, and brown spheres, respectively.

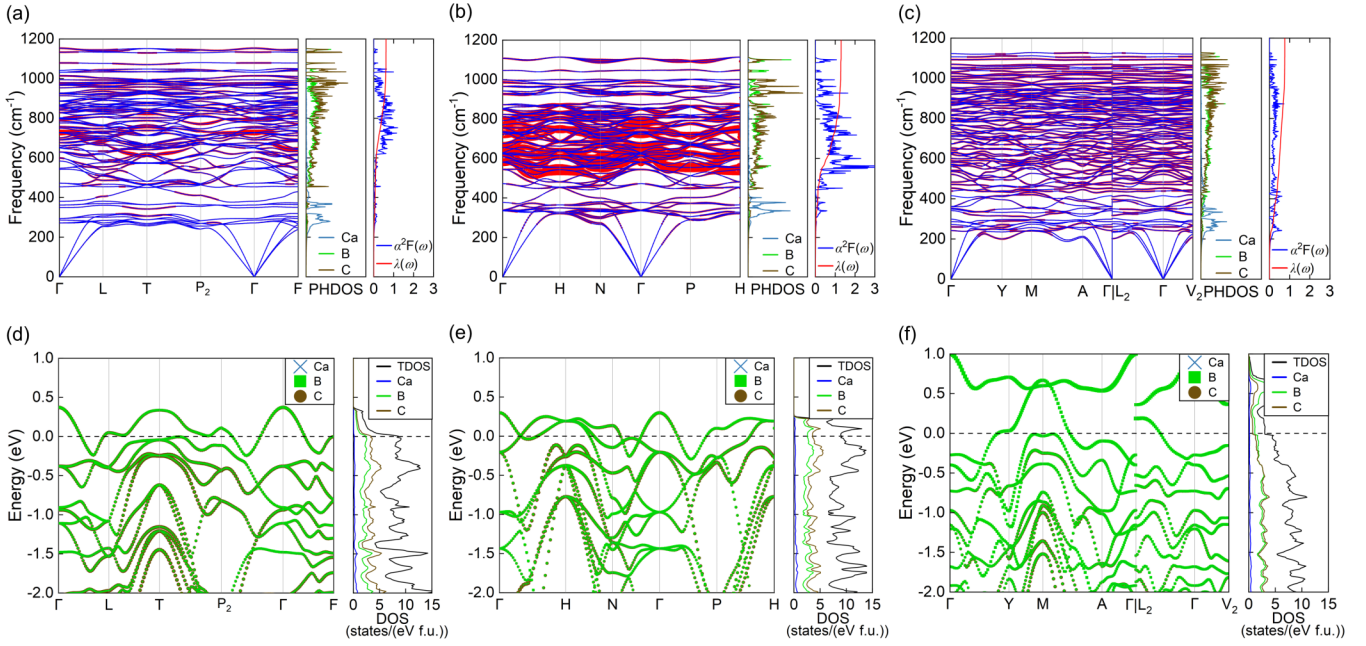


FIG. 4. Phonon dispersion curves, projected phonon density of states (PHDOS), Eliashberg spectral function  $\alpha^2F(\omega)$  and EPC integral  $\lambda(\omega)$  of (a)  $R3m$   $\text{Ca}_4\text{B}_9\text{C}_{14}$ , (b)  $I43m$   $\text{Ca}_4\text{B}_{10}\text{C}_{13}$ , and (c)  $Cm$   $\text{Ca}_4\text{B}_{11}\text{C}_{12}$  at 50 GPa. Phonon dispersion is represented by blue thin lines, decorated with the respective phonon linewidth  $\gamma_{vq}$  in red circles. Fat electron band structure, projected density of states (PDOS), and total density of states (TDOS) of (d)  $R3m$   $\text{Ca}_4\text{B}_9\text{C}_{14}$ , (e)  $I43m$   $\text{Ca}_4\text{B}_{10}\text{C}_{13}$ , and (f)  $Cm$   $\text{Ca}_4\text{B}_{11}\text{C}_{12}$  at 50 GPa.

that the  $T_c$  of  $\text{Ca}_4\text{B}_x\text{C}_{23-x}$  ( $x = 9-11$ ) is sensitive to boron content, which can influence the phonon softening and  $N(E_F)$  of phases.

Given that B-C clathrates may be synthesized at high pressure and depressurized to moderate even atmospheric pressure [17,18,63], we also calculated the superconductivity of five  $\text{Ca}_4\text{B}_x\text{C}_{23-x}$  phases under different pressure conditions as shown in Table S4 [52] and summarized in Fig. 5. As a result,

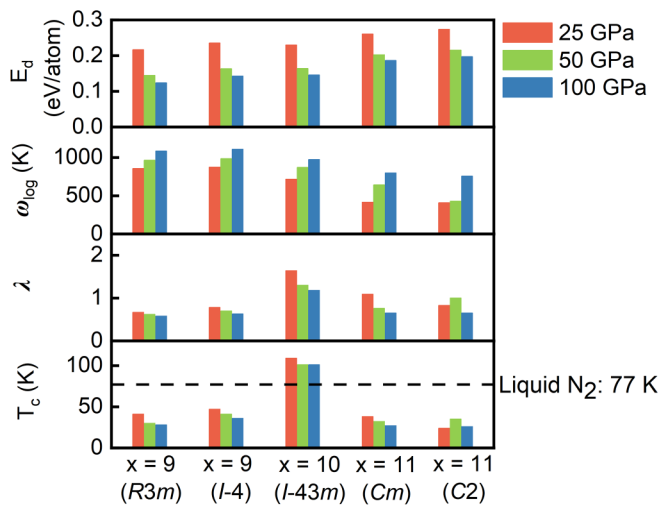


FIG. 5. Calculated enthalpy above convex hull ( $E_d$ ), logarithmic average frequency  $\omega_{\log}$ , EPC constant  $\lambda$ , and  $T_c$  of  $R3m$   $\text{Ca}_4\text{B}_9\text{C}_{14}$ ,  $I4$   $\text{Ca}_4\text{B}_9\text{C}_{14}$ ,  $I43m$   $\text{Ca}_4\text{B}_{10}\text{C}_{13}$ ,  $Cm$   $\text{Ca}_4\text{B}_{11}\text{C}_{12}$ , and  $C2$   $\text{Ca}_4\text{B}_{11}\text{C}_{12}$  at different pressure conditions, respectively. Here, the values of  $T_c$  are estimated using the Migdal-Eliashberg approach by setting the screened Coulomb potential  $\mu^* = 0.10$ .

these five phases can keep cage structures and are dynamically stable from 25 to 100 GPa (see Figs. S7–S9 [52]), and their  $E_d$  show a decreasing trend as the pressure increases in this pressure range as shown in Fig. 5. As expected, with pressure increases the length of B-C bond decreases, significantly hardening the phonon modes as shown in Fig. 4 and Figs. S11–S13 [52]. Therefore,  $\omega_{\log}$  increases and  $\lambda$  decreases, and in the competition between  $\omega_{\log}$  and  $\lambda$ ,  $\lambda$  plays the dominant role, which leads to the  $T_c$ s having a consistent trend with pressure as  $\lambda$ . However,  $C2$   $\text{Ca}_4\text{B}_{11}\text{C}_{12}$  is an exception, as seen in Fig. 5;  $\lambda$  increased at 25–50 GPa, leading the value of  $T_c$  at 50 GPa to be larger than that at 25 GPa.

A further question is, can any of these superconducting phases be quenched to ambient pressure? By calculating the phonon spectra of these superconducting phases, we found that three phases ( $R3m$   $\text{Ca}_4\text{B}_9\text{C}_{14}$ ,  $I4$   $\text{Ca}_4\text{B}_9\text{C}_{14}$ , and  $I43m$   $\text{Ca}_4\text{B}_{10}\text{C}_{13}$ ) maintain dynamical stability at ambient pressure. In comparison, the other two phases ( $Cm$   $\text{Ca}_4\text{B}_{11}\text{C}_{12}$  and  $C2$   $\text{Ca}_4\text{B}_{11}\text{C}_{12}$ ) are dynamically unstable at ambient pressure. It indicates that the three dynamically stable superconducting phases have the potential to quench to ambient pressure. By solving the isotropic Eliashberg equation, we estimated the values of  $T_c$  for  $R3m$   $\text{Ca}_4\text{B}_9\text{C}_{14}$  (63 K),  $I4$   $\text{Ca}_4\text{B}_9\text{C}_{14}$  (79 K), and  $I43m$   $\text{Ca}_4\text{B}_{10}\text{C}_{13}$  (107 K) at ambient pressure.

#### IV. CONCLUSIONS

In summary, we explored the stability and superconductivity of ternary  $\text{Ca}_4\text{B}_x\text{C}_{23-x}$  ( $x = 0-23$ ) clathrates at 25–100 GPa. A total of 8388608 possible structures of  $\text{Ca}_4\text{B}_x\text{C}_{23-x}$  were considered. After symmetry screening, B-B bond screening, and structure deduplication, 351 unique



candidate structures remained. Based on the DFT calculations, we identified five metallic, thermodynamically metastable phases that preserved good cage characteristics at 25–100 GPa. Their superconductivity was demonstrated by the Migdal-Eliashberg theory and the DFPT calculations. These include  $R3m$   $\text{Ca}_4\text{B}_9\text{C}_{14}$  with  $T_c$  of  $\sim 28$ – $41$  K,  $I\bar{4}$   $\text{Ca}_4\text{B}_9\text{C}_{14}$  with  $T_c \sim 36$ – $47$  K,  $I\bar{4}3m$   $\text{Ca}_4\text{B}_{10}\text{C}_{13}$  with  $T_c$  of  $\sim 101$ – $109$  K,  $Cm$   $\text{Ca}_4\text{B}_{11}\text{C}_{12}$  with  $T_c$  of  $\sim 27$ – $38$  K, and  $C2$   $\text{Ca}_4\text{B}_{11}\text{C}_{12}$  with  $T_c \sim 24$ – $35$  K across 25–100 GPa. The high  $\lambda$  and  $T_c$  values arise from the strong coupling between the B-C electronic states at the Fermi level and the phonon modes

of the B-C atoms. Our findings suggest that metal doping and boron substitution in carbon clathrates are effective strategies for exploring high-temperature superconductors.

## ACKNOWLEDGMENTS

This work is supported by the National Natural Science Foundation of China (Grant No. 12374015). Shaorong Fang and Tianfu Wu from the Information and Network Center of Xiamen University are acknowledged for their help with the GPU computing.

- [1] Z. Li, X. He, C. Zhang, X. Wang, S. Zhang, Y. Jia, S. Feng, K. Lu, J. Zhao, J. Zhang, B. Min, Y. Long, R. Yu, L. Wang, M. Ye, Z. Zhang, V. Prakapenka, S. Chariton, P. A. Ginsberg, J. Bass, S. Yuan, H. Liu, and C. Jin, Superconductivity above 200 K discovered in superhydrides of calcium, *Nat. Commun.* **13**, 2863 (2022).
- [2] L. Ma, K. Wang, Y. Xie, X. Yang, Y. Wang, M. Zhou, H. Liu, X. Yu, Y. Zhao, H. Wang, G. Liu, and Y. Ma, High-temperature superconducting phase in clathrate calcium hydride  $\text{CaH}_6$  up to 215 K at a pressure of 172 GPa, *Phys. Rev. Lett.* **128**, 167001 (2022).
- [3] P. Kong, V. S. Minkov, M. A. Kuzovnikov, A. P. Drozdov, S. P. Besedin, S. Mozaffari, L. Balicas, F. F. Balakirev, V. B. Prakapenka, S. Chariton, D. A. Knyazev, E. Greenberg, and M. I. Eremets, Superconductivity up to 243 K in the yttrium-hydrogen system under high pressure, *Nat. Commun.* **12**, 5075 (2021).
- [4] Y. Wang, K. Wang, Y. Sun, L. Ma, Y. Wang, B. Zou, G. Liu, M. Zhou, and H. Wang, Synthesis and superconductivity in yttrium superhydrides under high pressure, *Chin. Phys. B* **31**, 106201 (2022).
- [5] A. P. Drozdov, P. P. Kong, V. S. Minkov, S. P. Besedin, M. A. Kuzovnikov, S. Mozaffari, L. Balicas, F. F. Balakirev, D. E. Graf, V. B. Prakapenka, E. Greenberg, D. A. Knyazev, M. Tkacz, and M. I. Eremets, Superconductivity at 250 K in lanthanum hydride under high pressures, *Nature (London)* **569**, 528 (2019).
- [6] M. Somayazulu, M. Ahart, A. K. Mishra, Z. M. Geballe, M. Baldini, Y. Meng, V. V. Struzhkin, and R. J. Hemley, Evidence for superconductivity above 260 K in lanthanum superhydride at megabar pressures, *Phys. Rev. Lett.* **122**, 027001 (2019).
- [7] K. Dolui, L. J. Conway, C. Heil, T. A. Strobel, R. P. Prasankumar, and C. J. Pickard, Feasible route to high-temperature ambient-pressure hydride superconductivity, *Phys. Rev. Lett.* **132**, 166001 (2024).
- [8] A. Sanna, T. F. T. Cerqueira, Y.-W. Fang, I. Errea, A. Ludwig, and M. A. L. Marques, Prediction of ambient pressure conventional superconductivity above 80 K in hydride compounds, *npj Comput. Mater.* **10**, 44 (2024).
- [9] F. Zheng, Z. Zhang, Z. Wu, S. Wu, Q. Lin, R. Wang, Y. Fang, C.-Z. Wang, V. Antropov, Y. Sun, and K.-M. Ho, Prediction of ambient pressure superconductivity in cubic ternary hydrides with  $\text{MH}_6$  octahedra, *Mater. Today Phys.* **42**, 101374 (2024).
- [10] Y. He, J. Lu, X. Wang, and J.-J. Shi, Phonon-mediated superconductivity in the metal-bonded perovskite  $\text{Al}_4\text{H}$  up to 54 K under ambient pressure, *Phys. Rev. B* **108**, 054515 (2023).
- [11] Y. He and J.-j. Shi, Few-hydrogen high- $T_c$  superconductivity in  $(\text{Be}_4)_2\text{H}$  nanosuperlattice with promising ductility under ambient pressure, *Nano Lett.* **23**, 8126 (2023).
- [12] C. Tian, Y. He, Y.-h. Zhu, J. Du, S.-m. Liu, W.-h. Guo, H.-x. Zhong, J. Lu, X. Wang, and J.-j. Shi, Few-hydrogen metal-bonded perovskite superconductor  $\text{MgHCu}_3$  with a critical temperature of 42 K under atmospheric pressure, *Adv. Funct. Mater.* **34**, 2304919 (2024).
- [13] S. Lu, H. Liu, I. I. Naumov, S. Meng, Y. Li, J. S. Tse, B. Yang, and R. J. Hemley, Superconductivity in dense carbon-based materials, *Phys. Rev. B* **93**, 104509 (2016).
- [14] Y.-L. Hai, M.-J. Jiang, H.-L. Tian, G.-H. Zhong, W.-J. Li, C.-L. Yang, X.-J. Chen, and H.-Q. Lin, Superconductivity above 100 K predicted in carbon-cage network, *Adv. Sci.* **10**, 2303639 (2023).
- [15] K. Sano, Y. Masuda, and H. Ito, Superconductivity of carbon compounds with sodalite structure, *J. Phys. Soc. Jpn.* **91**, 083703 (2022).
- [16] T. Zeng, R. Hoffmann, R. Nesper, N. W. Ashcroft, T. A. Strobel, and D. M. Proserpio, Li-Filled, B-substituted carbon clathrates, *J. Am. Chem. Soc.* **137**, 12639 (2015).
- [17] L. Zhu, G. M. Borstad, H. Liu, P. A. Guńka, M. Guertel, J.-A. Dolyniuk, Y. Meng, E. Greenberg, V. B. Prakapenka, B. L. Chaloux, A. Epshteyn, R. E. Cohen, and T. A. Strobel, Carbon-boron clathrates as a new class of  $\text{sp}^3$ -bonded framework materials, *Sci. Adv.* **6**, eaay8361 (2020).
- [18] L. Zhu, H. Liu, M. Somayazulu, Y. Meng, P. A. Guńka, T. B. Shiell, C. Kenney-Benson, S. Chariton, V. B. Prakapenka, H. Yoon, J. A. Horn, J. Paglione, R. Hoffmann, R. E. Cohen, and T. A. Strobel, Superconductivity in  $\text{SrB}_3\text{C}_3$  clathrate, *Phys. Rev. Res.* **5**, 013012 (2023).
- [19] S. Di Cataldo, S. Qulaghasi, G. B. Bachelet, and L. Boeri, High- $T_c$  superconductivity in doped boron-carbon clathrates, *Phys. Rev. B* **105**, 064516 (2022).
- [20] J.-N. Wang, X.-W. Yan, and M. Gao, High-temperature superconductivity in  $\text{SrB}_3\text{C}_3$  and  $\text{BaB}_3\text{C}_3$  predicted from first-principles anisotropic Migdal-Eliashberg theory, *Phys. Rev. B* **103**, 144515 (2021).
- [21] P. Zhang, X. Li, X. Yang, H. Wang, Y. Yao, and H. Liu, Path to high- $T_c$  superconductivity via Rb substitution of guest

- metal atoms in the  $\text{SrB}_3\text{C}_3$  clathrate, *Phys. Rev. B* **105**, 094503 (2022).
- [22] T.-T. Gai, P.-J. Guo, H.-C. Yang, Y. Gao, M. Gao, and Z.-Y. Lu, Van Hove singularity induced phonon-mediated superconductivity above 77 K in hole-doped  $\text{SrB}_3\text{C}_3$ , *Phys. Rev. B* **105**, 224514 (2022).
- [23] N. Geng, K. P. Hilleke, L. Zhu, X. Wang, T. A. Strobel, and E. Zurek, Conventional high-temperature superconductivity in metallic, covalently bonded, binary-guest C–B clathrates, *J. Am. Chem. Soc.* **145**, 1696 (2023).
- [24] Q. Duan, L. Zhan, J. Shen, X. Zhong, and C. Lu, Predicting superconductivity near 70 K in 1166-type boron-carbon clathrates at ambient pressure, *Phys. Rev. B* **109**, 054505 (2024).
- [25] Y. Sun and L. Zhu, Hydride units filled B-C clathrate: A new pathway for high-temperature superconductivity at ambient pressure, *Commun. Phys.* **7**, 324 (2024).
- [26] J. Li, J. Yue, S. Guo, A. Zhang, L. Zhu, H. Song, Z. Liu, Y. Liu, and T. Cui, High-temperature superconductivity of boron-carbon clathrates at ambient pressure, *Phys. Rev. B* **109**, 144509 (2024).
- [27] B. Li, Y. Cheng, C. Zhu, J. Cheng, and S. Liu, Superconductivity near 70 K in boron-carbon clathrates  $\text{MB}_2\text{C}_8$  ( $M = \text{Na}, \text{K}, \text{Rb}, \text{Cs}$ ) at ambient pressure, *Phys. Rev. B* **109**, 184517 (2024).
- [28] X. Li, X. Yong, M. Wu, S. Lu, H. Liu, S. Meng, J. S. Tse, and Y. Li, Hard BN clathrate superconductors, *J. Phys. Chem. Lett.* **10**, 2554 (2019).
- [29] Y. Hai, H. Tian, M. Jiang, W. Li, G. Zhong, C. Yang, X. Chen, and H. Lin, Improving  $T_c$  in sodalite-like boron-nitrogen compound  $\text{M}_2(\text{BN})_6$ , *Mater. Today Phys.* **25**, 100699 (2022).
- [30] X. Cui, K. P. Hilleke, X. Wang, M. Lu, M. Zhang, E. Zurek, W. Li, D. Zhang, Y. Yan, and T. Bi,  $\text{RbB}_3\text{Si}_3$ : An alkali metal borosilicide that is metastable and superconducting at 1 atm, *J. Phys. Chem. C* **124**, 14826 (2020).
- [31] A. J. Karttunen, T. F. Fässler, M. Linnolahti, and T. A. Pakkanen, Structural principles of semiconducting group 14 clathrate frameworks, *Inorg. Chem.* **50**, 1733 (2011).
- [32] M. O’Keeffe, G. B. Adams, and O. F. Sankey, Duals of Frank-Kasper structures as C, Si and Ge clathrates: Energetics and structure, *Philos. Mag. Lett.* **78**, 21 (1998).
- [33] J.-T. Wang, C. Chen, D.-S. Wang, H. Mizuseki, and Y. Kawazoe, Phase stability of carbon clathrates at high pressure, *J. Appl. Phys.* **107**, 063507 (2010).
- [34] R. Nesper, K. Vogel, and P. E. Blöchl, Hypothetical carbon modifications derived from zeolite frameworks, *Angew. Chem. Int. Ed.* **32**, 701 (1993).
- [35] X. Blase, P. Gillet, A. San Miguel, and P. Mélinon, Exceptional ideal strength of carbon clathrates, *Phys. Rev. Lett.* **92**, 215505 (2004).
- [36] D. Connétable, First-principles calculations of carbon clathrates: Comparison to silicon and germanium clathrates, *Phys. Rev. B* **82**, 075209 (2010).
- [37] F. Colonna, A. Fasolino, and E. J. Meijer, Structure and thermodynamic stability of carbon clathrates: A Monte Carlo study, *Solid State Commun.* **152**, 180 (2012).
- [38] I. A. Baburin, D. M. Proserpio, V. A. Saleev, and A. V. Shipilova, From zeolite nets to  $sp^3$  carbon allotropes: A topology-based multiscale theoretical study, *Phys. Chem. Chem. Phys.* **17**, 1332 (2015).
- [39] F. J. Ribeiro, P. Tangney, S. G. Louie, and M. L. Cohen, Hypothetical hard structures of carbon with cubic symmetry, *Phys. Rev. B* **74**, 172101 (2006).
- [40] B. Eisenmann, H. Schäfer, and R. Zagler, Die verbindungen  $\text{A}^{\text{II}}_8\text{B}^{\text{III}}_{16}\text{B}^{\text{IV}}_{30}$  ( $\text{A}^{\text{II}} \equiv \text{Sr}, \text{Ba}$ ;  $\text{B}^{\text{III}} \equiv \text{Al}, \text{Ga}$ ;  $\text{B}^{\text{IV}} \equiv \text{Si}, \text{Ge}, \text{Sn}$ ) und ihre käfigstrukturen, *J. Less-Common Met.* **118**, 43 (1986).
- [41] T. Bi, B. T. Eggers, R. E. Cohen, B. J. Campbell, and T. Strobel, Computational screening and stabilization of boron-substituted type-I and type-II carbon clathrates, *J. Am. Chem. Soc.* **146**, 7985 (2024).
- [42] Z. Cui, X. Zhang, Y. Sun, Y. Liu, and G. Yang, Prediction of novel boron-carbon based clathrates, *Phys. Chem. Chem. Phys.* **24**, 16884 (2022).
- [43] C. Zhang, H. Tang, C. Pan, H. Jiang, H.-J. Sun, K.-M. Ho, and C.-Z. Wang, Machine learning guided discovery of superconducting calcium borocarbides, *Phys. Rev. B* **108**, 024512 (2023).
- [44] J. P. Perdew, K. Burke, and M. Ernzerhof, Generalized gradient approximation made simple, *Phys. Rev. Lett.* **77**, 3865 (1996).
- [45] P. E. Blöchl, Projector augmented-wave method, *Phys. Rev. B* **50**, 17953 (1994).
- [46] G. Kresse and J. Furthmüller, Efficient iterative schemes for *ab initio* total-energy calculations using a plane-wave basis set, *Phys. Rev. B* **54**, 11169 (1996).
- [47] A. Togo, L. Chaput, T. Tadano, and I. Tanaka, Implementation strategies in phonopy and phono3py, *J. Phys.: Condens. Matter* **35**, 353001 (2023).
- [48] S. Baroni, S. de Gironcoli, A. Dal Corso, and P. Giannozzi, Phonons and related crystal properties from density-functional perturbation theory, *Rev. Mod. Phys.* **73**, 515 (2001).
- [49] A. Dal Corso, Pseudopotentials periodic table: From H to Pu, *Comput. Mater. Sci.* **95**, 337 (2014).
- [50] P. Giannozzi, O. Andreussi, T. Brumme, O. Bunau, M. Buongiorno Nardelli, M. Calandra, R. Car, C. Cavazzoni, D. Ceresoli, M. Cococcioni, N. Colonna, I. Carnimeo, A. Dal Corso, S. de Gironcoli, P. Delugas, R. A. DiStasio, A. Ferretti, A. Floris, G. Fratesi, G. Fugallo *et al.*, Advanced capabilities for materials modelling with Quantum ESPRESSO, *J. Phys.: Condens. Matter* **29**, 465901 (2017).
- [51] P. Giannozzi, S. Baroni, N. Bonini, M. Calandra, R. Car, C. Cavazzoni, D. Ceresoli, G. L. Chiarotti, M. Cococcioni, I. Dabo, A. Dal Corso, S. de Gironcoli, S. Fabris, G. Fratesi, R. Gebauer, U. Gerstmann, C. Gougoussis, A. Kokalj, M. Lazzeri, L. Martin-Samos *et al.*, QUANTUM ESPRESSO: A modular and open-source software project for quantum simulations of materials, *J. Phys.: Condens. Matter* **21**, 395502 (2009).
- [52] See Supplemental Material at <http://link.aps.org/supplemental/10.1103/PhysRevB.110.214106> for notes, figures, tables, and which includes Refs. [41,43,75–85].
- [53] W. L. McMillan, Transition temperature of strong-coupled superconductors, *Phys. Rev.* **167**, 331 (1968).
- [54] R. C. Dynes, McMillan’s equation and the  $T_c$  of superconductors, *Solid State Commun.* **10**, 615 (1972).
- [55] P. B. Allen and R. C. Dynes, Transition temperature of strong-coupled superconductors reanalyzed, *Phys. Rev. B* **12**, 905 (1975).
- [56] F. Marsiglio, M. Schossmann, and J. P. Carbotte, Iterative analytic continuation of the electron self-energy to the real axis, *Phys. Rev. B* **37**, 4965 (1988).



- [57] G. M. Éliashberg, Interactions between electrons and lattice vibrations in a superconductor, *J. Exptl. Theoret. Phys. (U.S.S.R.)* **38**, 966 (1960) [*Sov. Phys. JETP* **11**, 696 (1960)].
- [58] R. Szcześniak, The numerical solution of the imaginary-axis Eliashberg equations, *Acta Phys. Pol. A* **109**, 179 (2006).
- [59] A. P. Durajski, R. Szcześniak, Y. Li, C. Wang, and J.-H. Cho, Isotope effect in superconducting lanthanum hydride under high compression, *Phys. Rev. B* **101**, 214501 (2020).
- [60] Z. Wu, Y. Sun, A. P. Durajski, F. Zheng, V. Antropov, K.-M. Ho, and S. Wu, Effect of doping on the phase stability and superconductivity in  $\text{LaH}_{10}$ , *Phys. Rev. Mater.* **7**, L101801 (2023).
- [61] J. Bauer, J.-F. Halet, and J.-Y. Saillard, Rare earth metal borocarbides: Examples of coordination compounds in solid-state chemistry, Dedicated to Professor Roald Hoffmann on the occasion of his 60<sup>th</sup> birthday, *Coord. Chem. Rev.* **178–180**, 723 (1998).
- [62] V. S. Urusov and T. N. Nadezhina, Frequency distribution and selection of space groups in inorganic crystal chemistry, *J. Struct. Chem.* **50**, 22 (2009).
- [63] T. A. Strobel, L. Zhu, P. A. Guńka, G. M. Borstad, and M. Guerette, A lanthanum-filled carbon–boron clathrate, *Angew. Chem. Int. Ed.* **60**, 2877 (2021).
- [64] W. Sun, S. T. Dacek, S. P. Ong, G. Hautier, A. Jain, W. D. Richards, A. C. Gamst, K. A. Persson, and G. Ceder, The thermodynamic scale of inorganic crystalline metastability, *Sci. Adv.* **2**, e1600225 (2016).
- [65] M. Aykol, S. S. Dwaraknath, W. Sun, and K. A. Persson, Thermodynamic limit for synthesis of metastable inorganic materials, *Sci. Adv.* **4**, eaaq0148 (2018).
- [66] K.-H. Klöss, D. Hinz-Hübner, and U. Ruschewitz, Über eine neue Modifikation des  $\text{Na}_2\text{C}_2$ , *Z. Anorg. Allg. Chem.* **628**, 2701 (2002).
- [67] K. I. Portnoi, V. M. Romashov, and L. N. Burobina, Constitution diagram of the system zirconium–boron, *Sov. Powder Metall. Met. Ceram.* **9**, 577 (1970).
- [68] V. Pavlyuk, V. Milashys, G. Dmytriv, and H. Ehrenberg, A new tetragonal structure type for  $\text{Li}_2\text{B}_2\text{C}$ , *Acta Crystallogr. Sec. C* **71**, 39 (2015).
- [69] I. Errea, M. Calandra, C. J. Pickard, J. R. Nelson, R. J. Needs, Y. Li, H. Liu, Y. Zhang, Y. Ma, and F. Mauri, Quantum hydrogen-bond symmetrization in the superconducting hydrogen sulfide system, *Nature (London)* **532**, 81 (2016).
- [70] I. Errea, F. Belli, L. Monacelli, A. Sanna, T. Koretsune, T. Tadano, R. Bianco, M. Calandra, R. Arita, F. Mauri, and J. A. Flores-Livas, Quantum crystal structure in the 250-kelvin superconducting lanthanum hydride, *Nature (London)* **578**, 66 (2020).
- [71] S.-W. Kim, K. Wang, S. Chen, L. J. Conway, G. L. Pascut, I. Errea, C. J. Pickard, and B. Monserrat, On the dynamical stability of copper-doped lead apatite, *npj Comput. Mater.* **10**, 16 (2024).
- [72] Y. Sun, F. Zhang, C.-Z. Wang, K.-M. Ho, I. I. Mazin, and V. Antropov, Electron-phonon coupling strength from *ab initio* frozen-phonon approach, *Phys. Rev. Mater.* **6**, 074801 (2022).
- [73] R. Wang, Y. Sun, F. Zhang, F. Zheng, Y. Fang, S. Wu, H. Dong, C.-Z. Wang, V. Antropov, and K.-M. Ho, High-throughput screening of strong electron–phonon couplings in ternary metal diborides, *Inorg. Chem.* **61**, 18154 (2022).
- [74] K.-P. Bohnen, R. Heid, and B. Renker, Phonon dispersion and electron-phonon coupling in  $\text{MgB}_2$  and  $\text{AlB}_2$ , *Phys. Rev. Lett.* **86**, 5771 (2001).
- [75] R. Schmitt, B. Blaschkowski, K. Eichele, and H. J. Meyer, Calcium tetraboride, Does it exist? Synthesis and properties of a carbon-doped calcium tetraboride that is isotopic with the known rare earth tetraborides, *Inorg. Chem.* **45**, 3067 (2006).
- [76] S. Shah and A. N. Kolmogorov, Stability and superconductivity of Ca–B phases at ambient and high pressure, *Phys. Rev. B* **88**, 014107 (2013).
- [77] Y.-L. Li, S.-N. Wang, A. R. Oganov, H. Gou, J. S. Smith, and T. A. Strobel, Investigation of exotic stable calcium carbides using theory and experiment, *Nat. Commun.* **6**, 6974 (2015).
- [78] P. Tsuppayakorn-ae, X. Yang, P. Pluengphon, W. Luo, R. Ahuja, and T. Bovornratanaraks, Route to high- $T_c$  superconductivity of  $\text{BC}_7$  via strong bonding of boron–carbon compound at high pressure, *Sci. Rep.* **10**, 18090 (2020).
- [79] A. Jay, O. Hardouin Duparc, J. Sjakste, and N. Vast, Theoretical phase diagram of boron carbide from ambient to high pressure and temperature, *J. Appl. Phys.* **125**, 185902 (2019).
- [80] A. Jayaraman, W. Klement, and G. C. Kennedy, Phase diagrams of calcium and strontium at high pressures, *Phys. Rev.* **132**, 1620 (1963).
- [81] H. Olijnyk and W. B. Holzapfel, Phase transitions in alkaline earth metals under pressure, *Phys. Lett. A* **100**, 191 (1984).
- [82] A. R. Oganov, Y. Ma, Y. Xu, I. Errea, A. Bergara, and A. O. Lyakhov, Exotic behavior and crystal structures of calcium under pressure, *Proc. Natl. Acad. Sci.* **107**, 7646 (2010).
- [83] T. Ishikawa, A. Ichikawa, H. Nagara, M. Geshi, K. Kusakabe, and N. Suzuki, Theoretical study of the structure of calcium in phases IV and V via *ab initio* metadynamics simulation, *Phys. Rev. B* **77**, 020101 (2008).
- [84] A. R. Oganov, J. Chen, C. Gatti, Y. Ma, Y. Ma, C. W. Glass, Z. Liu, T. Yu, O. O. Kurakevych, and V. L. Solozhenko, Ionic high-pressure form of elemental boron, *Nature (London)* **457**, 863 (2009).
- [85] U. Häussermann, S. I. Simak, R. Ahuja, and B. Johansson, Metal–nonmetal transition in the boron group elements, *Phys. Rev. Lett.* **90**, 065701 (2003).